JGR Oceans

RESEARCH ARTICLE
10.1029/2022JC019082

Tides, Internal and Near-Inertial Waves in the Yermak Pass at the Entrance of the Atlantic Water to the Arctic Ocean

Camila Artana[1], Christine Provost[2], Ramiro Ferrari[3], Clément Bricaud[4], Léa Poli[2], and Young-Hyang Park[2]

[1]Institut de Ciènces del Mar, Barcelona, Spain, [2]Laboratoire LOCEAN-IPSL, CNRS, IRD, MNHN, Sorbonne Universités, Paris, France, [3]NOVELTIS, Labège, France, [4]Mercator Ocean, Toulouse, France

Key Points:

- An anticyclonic residual circulation around the Yermak Plateau forced by the diurnal tide helps Atlantic Water penetrate into the Arctic
- Semi-diurnal stationary internal waves are observed in the Yermak Pass and could result from freely propagating semi-diurnal internal waves
- Freely propagating semi-diurnal internal waves are generated by diurnal barotropic tides on critical slopes around the plateau

Supporting Information:

Supporting Information may be found in the online version of this article.

Correspondence to:

C. Artana,
cartlod@locean-ipsl.upmc.fr

Citation:

Artana, C., Provost, C., Ferrari, R., Bricaud, C., Poli, L., & Park, Y.-H. (2022). Tides, internal and near-inertial waves in the Yermak Pass at the entrance of the Atlantic Water to the Arctic Ocean. *Journal of Geophysical Research: Oceans*, *127*, e2022JC019082. https://doi.org/10.1029/2022JC019082

Received 8 JUL 2022
Accepted 28 NOV 2022

Abstract In the crucial region of the Yermak Plateau where warm Atlantic water enters the Arctic ocean, we examined high frequency variations in the Yermak Pass Branch over a 34 months-long mooring data set. The mooring was ice covered only half of the time with ice-free periods both in summer and winter. We investigated the contribution of residual tidal currents to the low frequency flow of Atlantic Water (AW) and high frequency variations in velocity shears possibly associated with internal waves. High resolution model simulations including tides show that diurnal tide forced an anticyclonic circulation around the Yermak Plateau. This residual circulation helps the northward penetration of the AW into the Arctic. Tides should be taken into account when examining low frequency AW inflow. High frequency variations in velocity shears are mainly concentrated in a broad band around 12 hr in the Yermak Pass. Anticyclonic eddies, observed during ice-free conditions, modulate the shear signal. Semi-diurnal internal stationary waves dominate high frequency variations in velocity shears. The stationary waves could result from the interaction of freely propagating semi-diurnal internal waves generated by diurnal barotropic tides on critical slopes around the plateau. The breaking of the stationary waves with short length scales possibly contribute to mixing of AW at the entrance to the Arctic.

Plain Language Summary The Atlantic Water (AW) is the main source of heat and salt to the Arctic. The Yermak Plateau is a major obstacle to the flow. Tides are strong over the Yermak Plateau. Tides contribute to the mean flow helping the northward penetration of the AW around the Yermak Plateau. Tides play also key role in the generation of stationary waves likely important for mixing.

1. Introduction

The Atlantic Water (AW) flowing through the Fram Strait via the West Spitsbergen Current (WSC) is the main source of heat and salt for the Arctic Ocean. At the entrance to the Arctic the WSC splits into branches as it meets the Yermak Plateau (Figure 1a), a bathymetric feature stretching out into the Fram Strait north-west of Svalbard.

A significant portion of the AW navigates the central plateau following the 700-m isobath, through the Yermak Pass (the Yermak Pass Branch, YPB in Figure 1a), that is northward to 81.2°N before turning southeast and rejoining the onshore Svalbard Branch (SB in Figure 1a) around 10°E (Artana et al., 2022; Crews et al., 2019; Koenig et al., 2017). The YPB flow is characterized by strong intermittent flow pulses of 1–2 months duration in winter. Velocities associated with these intermittent vertically coherent flow pulses can reach 30 cm/s in the water column and 20 cm/s 50 m above the seafloor (Artana et al., 2022). The circulation in this region has been evolving rapidly since 2007 with a widespread intensification of the AW circulation over and around Yermak Plateau coincinding with an overall warming of the upper ocean layer (0–1,000m) (Athanase et al., 2021). In particular, AW recirculations toward Fram Strait (RB in Figure 1a) shifted further north while the Yermak Branch (YB) strengthened over the northern Yermak Plateau, occasionally crossing the plateau north of 81.6°N as a branch called Northern Branch (NB, dashed line in Figure 1a) hereafter.

Recently, Artana et al. (2022) analyzed the low-frequency variability (periods >50 hr) in 34 months (2017–2020) of mooring data gathered at 80.6°N and 7.26°E in the YPB (Figure 1). The comparison to mooring data obtained at the same location a decade earlier (2007–2008) when sea ice was abundant (mean sea ice concentration of 74% vs. 39% in 2017–2020) documented an increase in velocity variations of 40% compared to the 2007–2008 period. Year 2018 was exceptional with ice-free conditions over the entire year and an exacerbated mesoscale activity.

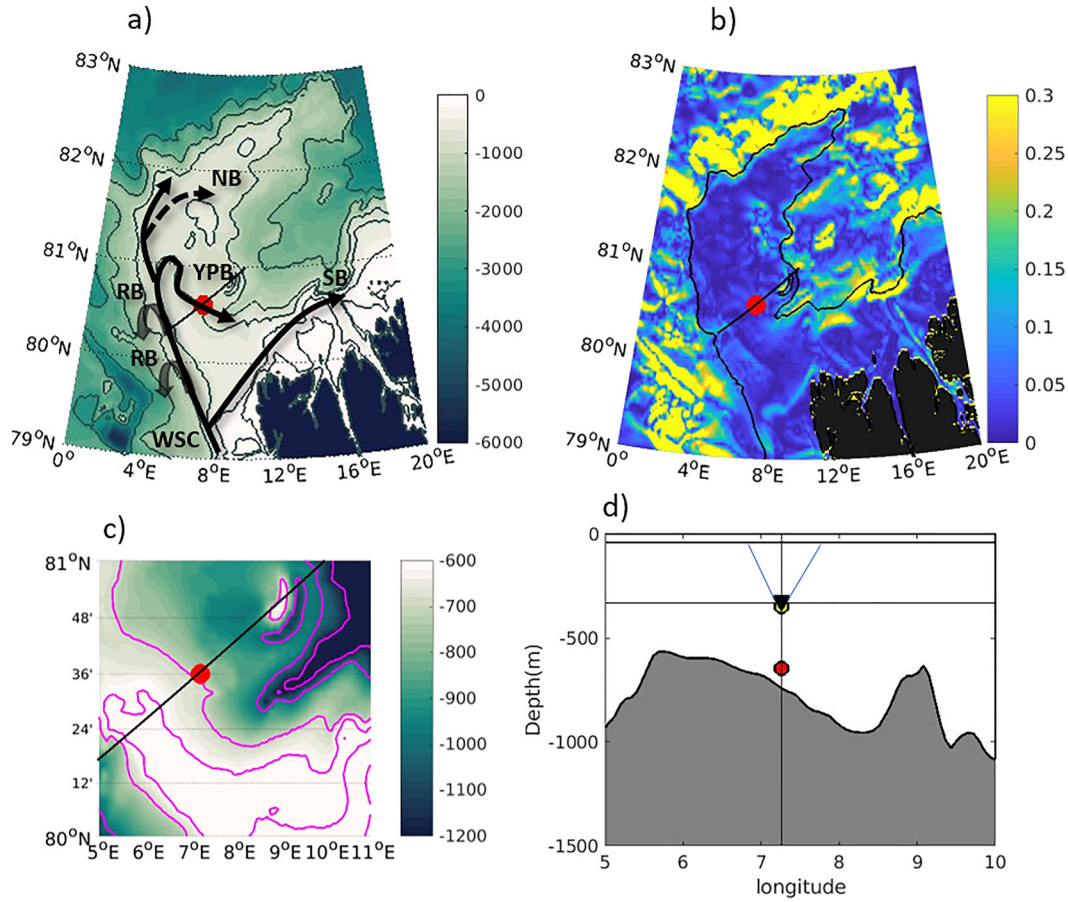

Figure 1. (a) Bathymetry around Yermak Plateau (color scale in m) from IBCAO (Jakobsson et al., 2012). Isolines mark the 100, 200, 700, 1,000, 2,000, and 3,000 m isobaths. The West Spitsbergen Current (WSC) splits into branches schematized with black arrows: recirculation branches (RB) to the west and south, and four branches navigating over the Yermak Plateau: the Svalbard Branch (SB), the Yermak Pass Branch (YPB), the Yermak Branch (YB) and the Northern Branch (NB) (dashed line) (adapted from Athanase et al., 2021). The red dot indicates the mooring location. (b) Bathymetry gradient (color scale in m/m). Black isoline marks the 1,000 m isobath. (c) Close up around the mooring site. Isolines are the 300, 500, 600, 700, 1,000, and 1,200 m isobaths. (d) Schematics of the mooring: the mooring carries an Aquadopp (red dot) at 645 m, a seabird microcat (yellow dot) and an upward-looking Acoustic Doppler Current Profiler (ADCP) at about 340 m (black triangle).The black horizontal lines indicate the ADCP range. Shaded area represents bathymetry along the black section indicated in (a–c).

The Yermak Plateau is known for large tidal currents. Tides may impact the inflow of Atlantic water into the Arctic Ocean through residual tidal currents. Padman et al. (1992) first hypothesized that residual tidal currents (either due to topographic rectification or baroclinic adjustment to tidal mixing) around the plateau could be important in advecting AW clockwise around the perimeter of the plateau. However, this issue has not received much attention.

The diurnal tides over the Yermak Plateau are unusually strong, periodically exceeding the strength of the semidiurnal currents (e.g., Hunkins, 1986; Padman et al., 1992). Significant internal wave production has been observed on the plateau (D'Asaro & Morison, 1992; Fer et al., 2015; Plueddemann, 1992), and has been linked to response of strong tidal currents over the bottom topography (Padman et al., 1992). The plateau lies poleward of the critical latitude ϕ_c of the major tidal constituents (latitude at which the tidal frequency matches the local inertial frequency), therefore precluding the linear generation of free baroclinic tides from barotropic tides (e.g., Vlasenko et al., 2003). Instead, the energy of the barotropic tide is transferred to short nonlinear internal waves like lee waves (e.g., Nakamura & Awaji, 2001; Rippeth et al., 2017; Vlasenko et al., 2003). In a recent study, Fer et al. (2020) evidenced solitons generated by the lee wave mechanism (Jackson et al., 2012) northeast of Svalbard (18°E, 81°N) where the bottom slope is steep (Figure 1b) and the cross-isobath diurnal tidal currents are large.

Table 1
Sampling Specificity of the Mooring Instruments

	Depth (m)	U	V	T	S	P	δt	δz
ADCP	340	x	x	x			2 hr	16 m
Seabird	348			x	x	x	10 min	–
Aquadopp	645	x	x			x	2 hr	–

Note. U: eastward velocity; V: northward velocity; T: temperature, S: salinity, P: pressure. δt: time sampling. δz: vertical sampling.

The surface expression of these nonlinear waves (NLIWs) can be observed with SAR images in the Arctic over steep topography (Kozlov et al., 2015).

A recent numerical study examined the generation of linear and nonlinear internal waves (including internal solitary waves) forced by subinertial tides over the Yermak Plateau (Urbancic et al., 2022). It was shown that the strength of the diurnal barotropic tide and the steepness of the slope are controlling factors in producing internal waves at higher harmonics and solitary waves. New mooring observations on the Southwestern slope of the Yermak Plateau documented strong barotropic diurnal tides triggering internal waves at higher harmonics, in particular at the semi-diurnal period (Wang et al., 2022). It is to be noted that the second harmonic (period 11.97 hr) of the diurnal tide is not subinertial over the Yermak Plateau and could freely propagate.

Wind-forced near-inertial waves (NIW) are another source of high frequencies potentially generating internal waves. Moored observations have shown extremely weak NIW kinetic energy under ice cover (Martini et al., 2014; Merrifield & Pinkel, 1996; Rainville & Woodgate, 2009). The presence of sea ice modulates the exchange of momentum between the atmosphere and the ocean and it has been hypothetized that the massive reduction in sea ice cover would lead to a more energetic internal wave field. However, recent studies, mostly in the Canada Basin, did not document significant changes (e.g., Dosser & Rainville, 2016; Guthrie & Morison, 2020; Guthrie et al., 2013; Lincoln et al., 2016). Among forcing mechanisms for NIWs are low-frequency flows either through loss of geostrophic balance (e.g., Alford et al., 2016; Nagai et al., 2015) or through interactions with seafloor topography including lee wave generation (e.g., Nikurashin & Ferrari, 2010).

We examined high frequency variations in the YPB using the 34 months-long data set presented in Artana et al. (2022). During those 34 months, sea ice concentration varied from 0% to 100% both in summer and winter, ocean low-frequency speeds ranged from 0 to 30 cm/s, wind speeds from 0 to 20 m/s and mixed-layer depths from 5 to 500 m (Artana et al., 2022). Thus the data set enabled to examine high frequency variations in ocean velocities and velocity shears within a large range of environmental conditions. The data set is complemented with numerical models to characterize tides over the Yermak Pass and investigate the contribution of residual tidal currents to the low frequency flow of Atlantic Water.

Section 2 revisits the ocean data set and presents complementary sources of information including models. Section 3 focuses on tides and their potential contribution to residual velocities. Section 4 analyses spectral characteristics of velocity shears and consider the relative contribution of stationary, upward and downward propagating shears to the total signal. Selected cases with specific environmental conditions are examined. Physical interpretation of shear characteristics in terms of internal waves are proposed. Section 5 summarizes and concludes.

2. Material

2.1. Mooring Data

The mooring data was acquired at 80.6°N and 7.26°E, in the Yermak Pass on the eastern flank of the Yermak Plateau from 25 September 2017 to 18 June 2020 (1,024 days, about 34 months) (Figures 1a and Artana et al., 2022). The seafloor is 725 m below sea level at the mooring location and rises to 580 m at the Yermak Plateau crest 10 km to the west of the mooring (Figures 1c and 1d). Whereas topography is rather smooth at the mooring location there is a deep canyon 20 km to the southeast and a seamount 20 km to the northeast (Figures 1b and 1c).

The mooring comprised 3 instruments: at about 340 m an upward-looking RDI 75 kHz Long Ranger Acoustic Doppler Current Profiler (ADCP) measuring velocity profiles (25 bins of 16 m each), at 348 m a seabird SBE37 measuring temperature salinity and pressure, and, at 645 m an Aquadopp currentmeter (Figure 1d). Measured variables and sampling interval are summarized in Table 1. For the ADCP, the 2 hr sampling resulted from averaging 24 pings obtained every 5 min. For the Aquadopp, it was a burst sampling every 2 hours.

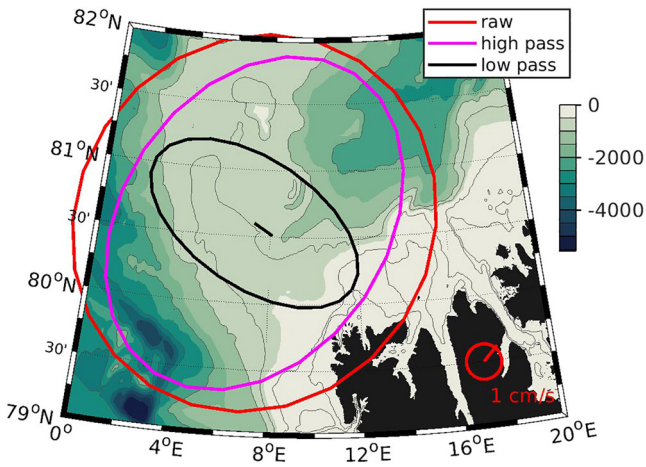

Figure 2. Mean velocity (arrow), velocity variance ellipses of the full-time resolution (red) and the high-pass (magenta) and low-pass (black) filtered (50-hr cutoff) velocities from the 34-month long time series at 645 m. Isolines are the 100, 200, 700, 1,000, 2,000, and 3,000 m isobaths.

The upper 50 m of the water column was not sampled as the vertical extent of the ADCP data was limited by the paucity of backscattering particles. The data return for all instruments (below 50 m) was close to 100%. Indeed, the only data gaps corresponded to 2% missing data between 100 and 50 m. A linear vertical interpolation was applied to fill the few gaps. Over the 34 months of measurements, the mooring stayed in a straight position: the seabird pressure had a mean of 355 db and a standard deviation of 2 db (largest drawdown of 35 db on 15 January 2020) (Artana et al., 2022).

Data were high-pass filtered using a fourth-order Butterworth filter with a 50-hr cutoff. High-pass filtered velocities show a rather barotropic structure and peak velocities in excess of 20 cm/s (Appendix A). High frequency variations (periods less than 50 hr) account for more than 70% of the total velocity variance. This is clearly illustrated with velocity variance ellipses at 645 m from the raw, high-pass and low-pass filtered velocities (Figure 2). Velocity variance ellipses reveal the magnitude, principal direction and anisotropic nature of the flow variability.

The raw velocity ellipse is rather circular, while the ellipse for the high-pass (respectively low-pass) velocities is elongated in the direction perpendicular (parallel) to isobaths (Figure 2). The ellipse main axis is 10.8 cm/s for the full time resolution velocities, 10.1 cm/s for the high-pass filtered velocities and only 6.6 cm/s for the low-pass filtered velocities (respectively red, magenta and black in Figure 2).

The inertial frequency at the mooring location corresponds to a period of 12.13 hr comprised within the semi-diurnal tide period range (M2 period 12.42 hr and S2 12.00 hr).

The power spectral density (PSD) of clockwise and counter clockwise currents at three depths illustrate the wealth of high frequency variability (Figures 3a and 3b). Currents show an enhanced variability at the diurnal and semidiurnal frequencies over the water column both in the clockwise and counterclockwise PSDs. The spectra also show significant peaks at numerous harmonics (e.g., 6.1, 6.2, 8.2, and 8.4 hr) (Figures 3a and 3b). The spectra of the high-pass filtered velocities show the dominance of CW (anticyclonic) motions at all observed depths around the semi-diurnal band, the diurnal band and in the harmonics (around 6 and 8 hr), as well as a decrease of energy with depth in CCW (cyclonic) motions (Figures 3c and 3d).

2.2. Models

To help interpreting the data we wielded several models.

We used the Arc5km2018 barotropic tidal model (Erofeeva & Egbert, 2020), a barotropic inverse tidal model on a 5-km grid which estimates tidal currents using 12 constituents; 5 semi-diurnal (M2, S2, K2, N2, 2N2), 4 diurnal (K1, 01, P1, Q1) and 3 nonlinear components around a 6-hr period (M4, MS4, MN4). The mooring latitude (inertial frequency of 12.13 hr) is poleward of the critical latitude of all components except for S2 (12.00 hr), K2 (11.97 hr) and the quarter of a day components.

The (1/12° grid) global operational system PSY4 from Mercator Ocean (Lellouche et al., 2018) helped put the observed low-frequency variations in a larger spatial and temporal context (Artana et al., 2022). Indeed, PSY4 exhibited rather decent skill (e.g., Athanase et al., 2019, 2020, 2021) in the western Nansen Basin in spite of inherent limitations. The model lacks tides and its resolution is not fully eddy resolving (grid size of 4 km and Rossby deformation radius of about 10 km in the region). It was suggested that the difference in mean velocities between PSY4 model and observations could result from residual tidal velocities that the model does not represent (Artana et al., 2022; Koenig et al., 2017).

To investigate further the residual tidal velocity hypothesis, we examined two eddy resolving simulations (spatial resolution of 1/36°, 75 levels) performed at Mercator Ocean with the same global general circulation model. They are 3 months-long twin simulations from January to March 2013 forced by the European Center for Medium-Range Weather Forecasts (ECMWF) Integrated Forecasting System (IFS) (spatial resolution 1/14° and

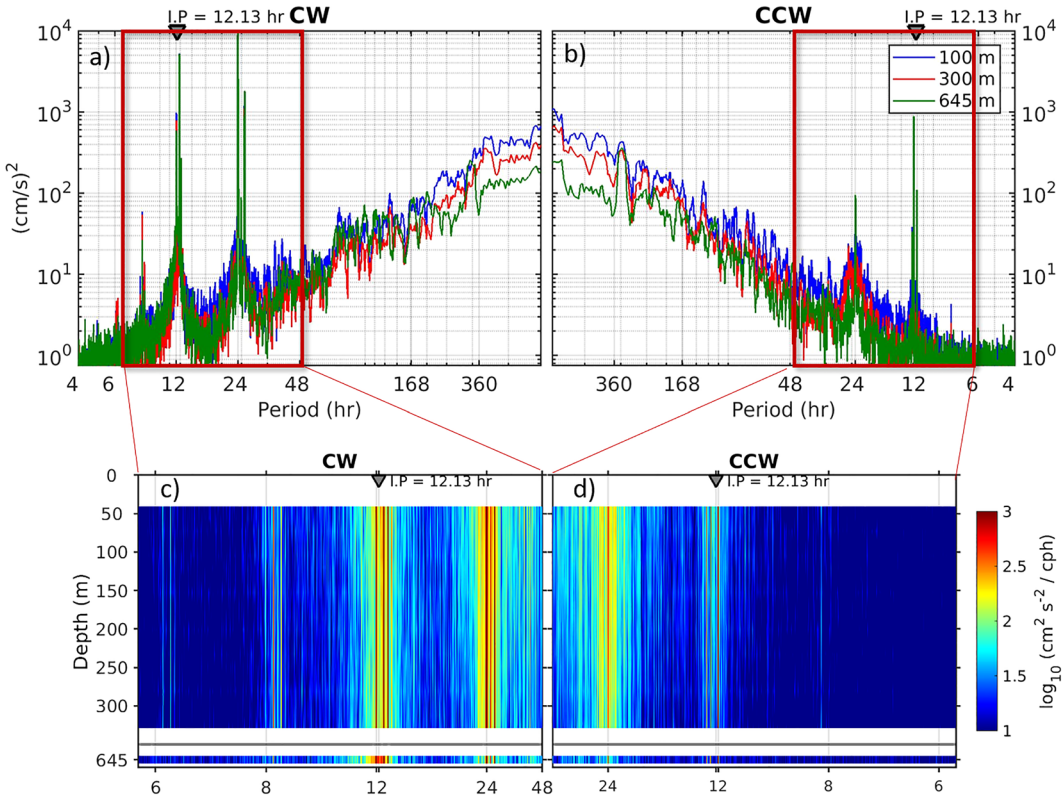

Figure 3. (a, b) Rotary spectra of velocity time series at 100, 300, and 645 m averaging over groups of four adjacent frequencies (2 hr resolution velocities). *x*-axis is period in hour (4–720 hr), *y*-axis is energy (in cm^2/s^2). CW, clockwise; CCW, counterclockwise. (c, d) Vertically coordinated frequency spectrum for the complex horizontal current: left (CW) clockwise rotation and right (CCW) counterclockwise rotation. Periods in hours. Velocities were high-pass filtered with a 50 hr-period cutoff (Section 2.1).

temporal resolution 1 hr) (https://www.ecmwf.int/en/publications/ifs-documentation). One simulation includes ocean tides with five harmonics (M2, K1, 01, S2, N2) and the Self Attraction and Loading (Arbic et al., 2004), while the other does not. These simulations are not contemporaneous with the mooring data and do not include data assimilation. However, they help look into the hypothesis of significant residual tidal currents.

2.3. Environmental Data and Selection of Study Cases

We used sea ice concentration from satellite data (EUMETSAT OSISAF product at daily temporal resolution and 3.125 km spatial resolution https://osi-saf.eumetsat.int/products:sea-ice-products) (Figure 4a). Hourly winds at 10 m were obtained from ERA5 reanalysis (Figure 4b) (https://cds.climate.copernicus.eu). Among other environmental conditions, we considered the maximum daily velocity from Arc5km2018 model (Figure 4c), the low-frequency ocean velocity amplitudes (50 hr low-pass filtered velocities at 100 m) (Figure 4d), the high-frequency pressure variations (Figure 4e) and mixed layer depths from PSY4 (Figure 4f).

The data span three winters with rather different conditions (Figure 4). In winter 2017–2018 the mooring location was ice free and very deep mixed layers developed. In winter 2018–2019 ice cover and mixed layers were variable while, in winter 2019–2020, the mooring location was mostly ice covered from November 2019 onward (Figure 4a). Pulses of low-frequency velocities reached 30 cm/s in winter (Figure 4d). Summers are in general characterized with milder winds, small mixed layer depths, small low-frequency ocean velocities, and an ice concentration close to 100% (Figure 4). Summer 2018 was exceptionally ice free. Maximum daily tide velocities, always above 10 cm/s peak at 30 cm/s and show a striking fortnightly modulation corresponding to the beat period between K1 and O1 (Figure 4c).

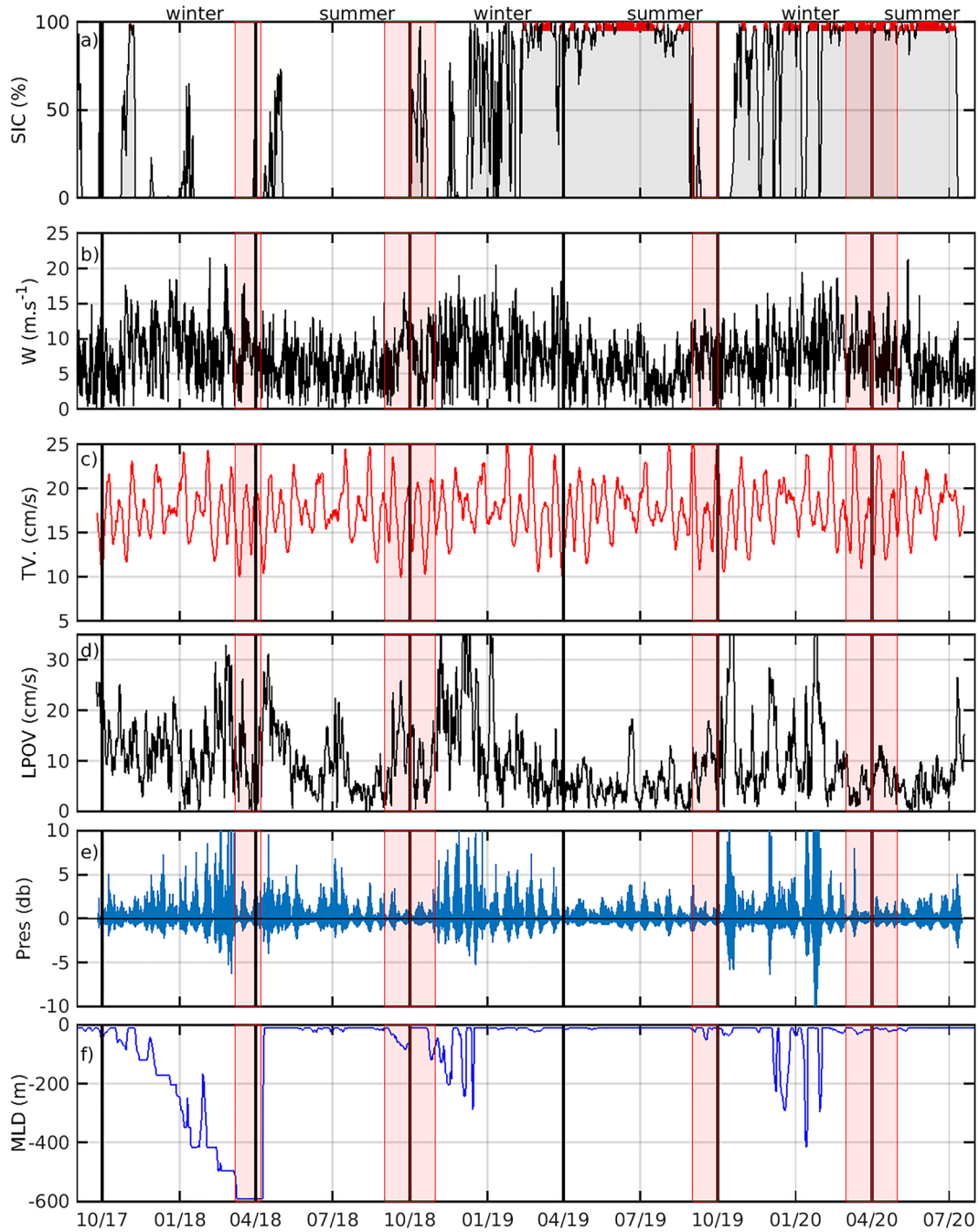

Figure 4. Time series of (a) sea ice concentration (SIC), (b) wind amplitude (W), (c) tidal velocity amplitude (TV), (d) 50-hr low-pass filtered ocean velocity amplitude at 100 m (LPOV), (e) 50 hr high-pass filtered pressure at 345 m and (f) mixed layer depth from PSY4. Selected periods are shaded in red. (Summer: April–September, winter: October–March).

Although pressure variations at the ADCP were small (std less than 2 db) in general, they could reach more than 10 m (Figure 4e) and contaminate vertical velocity shear estimates. We selected 3 months in winter and summer with small pressure variations as study cases. The six selected study cases examined in Section 4 are highlighted in red in Figure 4.

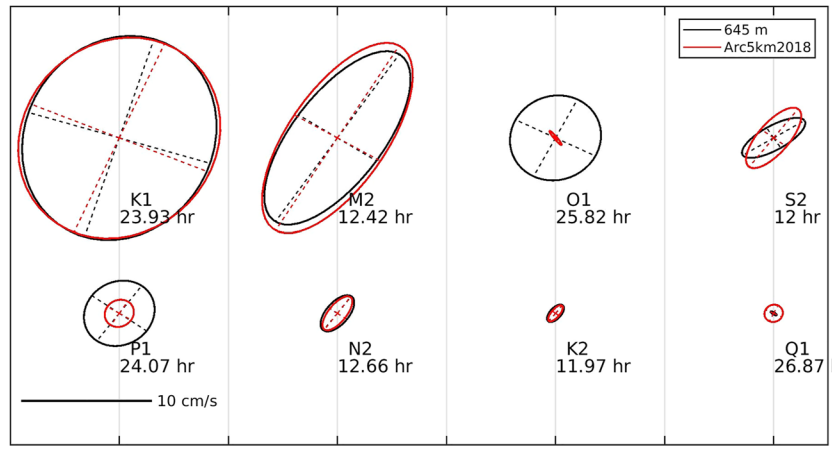

Figure 5. Tidal velocity ellipses of the eight major constituents estimated from the Aquadopp data (black) and the Arc5km2018 model (red).

3. Tidal Currents and Residual Velocities

3.1. Tidal Currents at the Mooring Site

We analyzed the tidal constituents present in the observed velocities using the T_TIDE Matlab toolbox (Pawlowicz et al., 2002) which is based on an early work by Foreman (1978). T_TIDE performs a harmonic analysis considering the known frequencies for up to 69 tidal constituents and calculates the relevant tidal ellipses parameters (major and minor axes, amplitudes, orientation, sense of rotation, direction and phase) with their confidence intervals. Estimates and uncertainties of tidal ellipse parameters (major axis, minor axis and angle of the major axis with respect to the north) of the first 12 constituents from the ADCP, Aquadopp and Arc5km2018 velocities obtained with the T-TIDE toolbox are detailed in the Supporting Information S1 and summarized in this section.

Figure 5 features tidal ellipses of the eight major constituents from the Aquadopp data and the Arc5km2018 model while Table 2 specifies the corresponding estimates and uncertainties of the tidal ellipses parameters. Ellipses of the constituents around the diurnal frequency (K1, O1, P1) are rather circular (major axis of 8.87, 3.70 and 2.92 cm/s, respectively) in contrast with ellipses from the semi-diurnal constituents (M2, S2, N2, K2) which are elongated in the direction perpendicular to isobaths (major axis of 8.59, 2.79 and 1.80 cm/s, respectively) (Figure 5 and Table 2). The Arc5km2018 model major constituents K1, M2, S2, N2, are close to the estimated values from observations whereas modeled O1 and P1 constituents are underestimated by a factor 4.5 and 2, respectively (Figure 5, Table 2). Differences between the Arc5km2018 and the observation-derived

Table 2
Tidal Ellipse Parameters: Major and Minor Axes (cm/s) and Angle (Degrees With Respect to the North in the Clockwise Direction) From the Aquadopp Currentmeter (Observations) and Arc5km2018 (Model)

	Major axis		Minor axis		Angle	
Constituent	Observations	Model	Observations	Model	Observations	Model
K1	8.87 (0.11)	8.78	7.28 (0.18)	7.52	73 (4)	67
M2	8.59 (0.11)	9.21	3.57 (0.19)	3.84	57 (1)	59
01	3.70 (0.11)	0.75	3.41 (0.18)	0.12	63 (22)	127
S2	2.79 (0.13)	3.11	1.02 (0.14)	1.23	32 (5)	53
P1	2.92 (0.12)	1.20	2.58 (0.16)	1.07	54 (18)	58
N2	1.81 (0.12)	1.71	0.89 (0.15)	0.71	54 (8)	55
K2	0.89 (0.13)	0.83	0.45 (0.16)	0.32	52 (16)	53
Q1	0.28 (0.16)	0.75	0.10 (0.11)	0.69	147 (31)	64

Note. Associated uncertainties are indicated in parentheses.

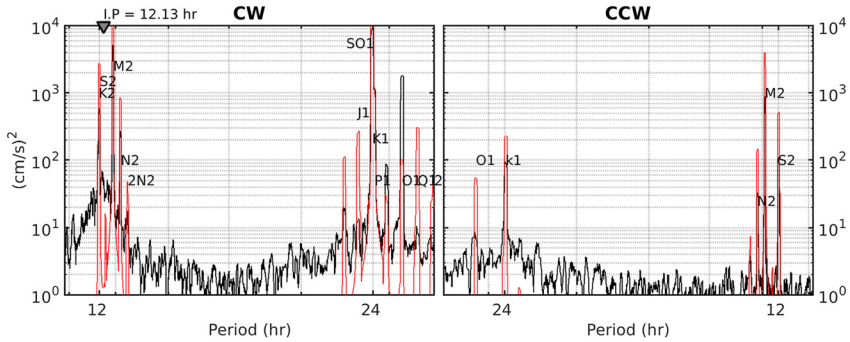

Figure 6. Rotary spectra of velocity time series from the Aquadopp at 645 m (black) and from Arc5km2018 model (red) averaging over groups of four adjacent frequencies (2 hr resolution velocities). *x*-axis is period in hour (11–28 hr), *y*-axis is energy (in cm^2/s^2). CW, clockwise; CCW, counterclockwise. Inertial period (I.P.) is 12.13 hr between S2 and M2 periods (12.00 and 12.42 hr, respectively).

ellipse parameters fall within the 95% confidence interval for the majority of the constituents (except O1 and P1) (Table 2).

The accordance between tidal constituents in the model and the observations is remarkable considering the model resolution (5 km) and the rather complex bathymetry in the vicinity of the mooring including a seamount to the northeast and canyon-type structure to the east of the mooring location (Figure 1b). The rotary spectra of the velocity time series confirm the good agreement between tidal components in observations and model except for O1 (smaller in the model) and Q1 (larger in the model) (left panel-CW- of Figure 6). Shallow-water constituents (interaction with bottom generates harmonics of the major constituents and compound tides) in Arc5km2018 are also comparable to observed ones (e.g., SO1 in the diurnal band). A broad-band increase in energy is centered around the inertial period in the observation-based CW spectrum, possibly associated with intermittent NIW at 645 m.

3.2. Tidal Currents Over the Yermak Plateau

Tidal current ellipses from Arc5km2018 over the Yermak Plateau help put tides at the mooring location in perspective (Figure 7). The tidal current ellipse at the mooring site (main axis of 10.1 cm/s) is rather small compared to other locations of the plateau. Tidal current ellipses increase in size over shallow topography on the

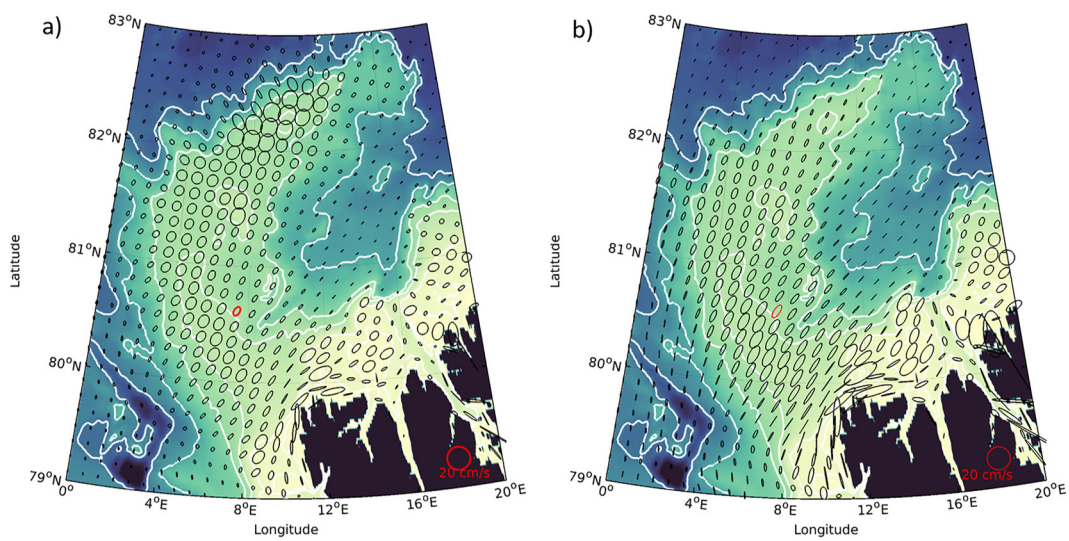

Figure 7. (a) Tidal current ellipses from Arc5km2018 (all 12 constituents from 24 September 2017 to 19 July 2020). The red ellipse is at the mooring location. The thick white isoline marks the 1,000 m isobath. (b) Same as (a) for M2 constituent.

continental slope and over the crest and the northern part of the plateau where the main axes of velocity variance ellipses reach 20 cm/s (Figure 7a). The semidiurnal tide ellipses are small in the northern Yermak Plateau (Figure 7b) where the diurnal tide dominates (Padman et al., 1992).

3.3. Residual Velocities

We compared mean velocities resulting from the twin simulations with a 1/36° resolution model, one simulation including tides with the five major harmonics M2, K1, O1, S2, and N2 (Section 2.2). The overall simulated tides were found acceptable (not shown), providing a good foundation for investigating residual currents in the region. Means were produced over different periods of time (1, 2, and 3 months) within the 3-month (January–March 2013) simulations and showed consistent similar features. As an example, we show velocities at 77 m (velocities are similar at depths). The winter flow is large with mean velocities exceeding 10 cm/s in the Yermak Pass (Figure 8a).

The two mean velocity fields differ along the steep slopes centered above the 1,000 m isobath, the simulation with tides producing an enhanced anticyclonic circulation around the plateau (Figures 8a–8c). The circulation is particularly intensified around the northern tip of the plateau, where tidal ellipses are large (cf. Figure 7), with residual velocities reaching 8 cm/s (Figures 8a–8c). The simulation with tides also leads to an increased mean southward flow (about +3 cm/s) along the eastern flank of the plateau. Along-isobath residual tidal currents encircling banks and islands have been observed in various places around the world. The combination of bottom friction and planetary vorticity as a tidal current flows across a topographic slope creates along-isobath mean circulation with the shallow water to the right of the current (in the northern hemisphere). The magnitude of the along-isobath rectified current depends on the steepness of the topographic slope and the strength of the cross-slope tidal oscillations (e.g., Loder, 1980; Wright & Loder, 1985; Zimmerman, 1978). Padman et al. (1992) first hypothesized that tidal rectification around the plateau could be a potentially important process in advecting AW clockwise around the perimeter of the plateau. They also suggested that diapycnal mixing due to tides could generate density gradients inducing geostrophically balanced alongslope baroclinic currents. The residual currents produced in the high resolution simulation were larger where diurnal tides are ample, suggesting that tidal rectification and mixing are key contributors to residual currents.

In contrast, a close up around the mooring location, a region with a rather complex topography (Figure 1c), shows that mean southeastward velocities in the YPB are smaller in the simulation with tides (Figures 8d and 8e). The tidal residual velocity at the mooring location is to the N-NE with an amplitude of 3–4 cm/s (Figure 8f). This direction and amplitude are consistent with residual velocities estimated in Koenig et al. (2017) comparing velocities from an operational model with no tides and mooring velocities. Thus, the YPB transport derived from a model without tides may be overestimated.

Overall, this exploratory comparison suggests to further investigate residual tidal currents around the plateau and to take tides into account when examining low frequency AW inflow.

4. Internal Waves and Near-Inertial Waves

4.1. Spectra of Baroclinic Velocities Over 3 Years

The rotary spectra of "baroclinic" current (ADCP depth average removed first) show dominant energy in the clockwise component with energy mainly concentrated around semi-diurnal band (Figure 9). This is in stark contrast with velocity spectra (Figure 3) which showed comparable energy levels around the semi-diurnal and diurnal periods.

Vertical shear components of the 50-hr high-pass filtered horizontal velocity were calculated from the ADCP data. Two-dimensional (2D) spectrum $\phi(k_z, \omega)$ of the shear vector, k_z being the vertical wave number and ω the frequency, provided information on the vertical scales (Text S2 in Supporting Information S1). In agreement with the "baroclinic" velocity spectra from Figure 9, the shear spectra show minor energy around the 24 hr period in the upward and downward panels compared to the semi-diurnal period (Figures S1 and S2 in Supporting Information S1). The dominant vertical scales is about 60 m (kz < 0.017) (Figure S2 in Supporting Information S1).

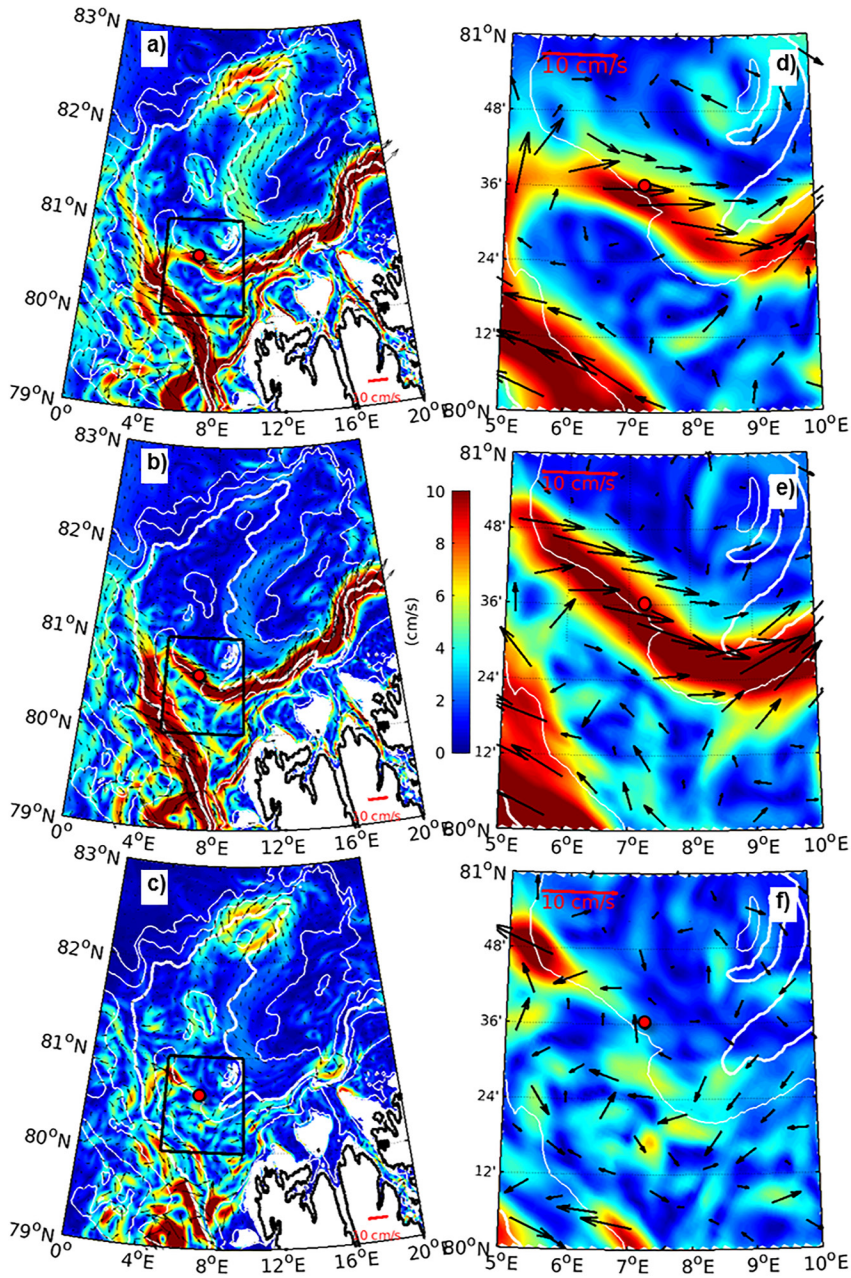

Figure 8. Model (1/36° resolution) mean velocities at 77 m from January 9 to 26 February 2013: with tides (a), no tides (b) and residual (c). Panels (d–f) are close up of (a–c) respectively on the Yermak Pass. Background is velocity amplitude. The thick white isoline marks the 1,000 m isobath.

The shear time series in the water column were decomposed into three components: a stationary, upward propagating and downward propagating shears following Park et al. (2004) methodology. The decomposition is analyzed for the cases selected in Section 2.3 corresponding to small ADCP vertical motions. The environmental characteristics of the 6 cases are summarized in Table 3.

Next section focuses on the month of September 2018 which featured active mesoscale background and a few intense wind bursts. In spite of the very active velocity field in September 2018 pressure variations at the ADCP did not exceed 2 db (Figure 4e).

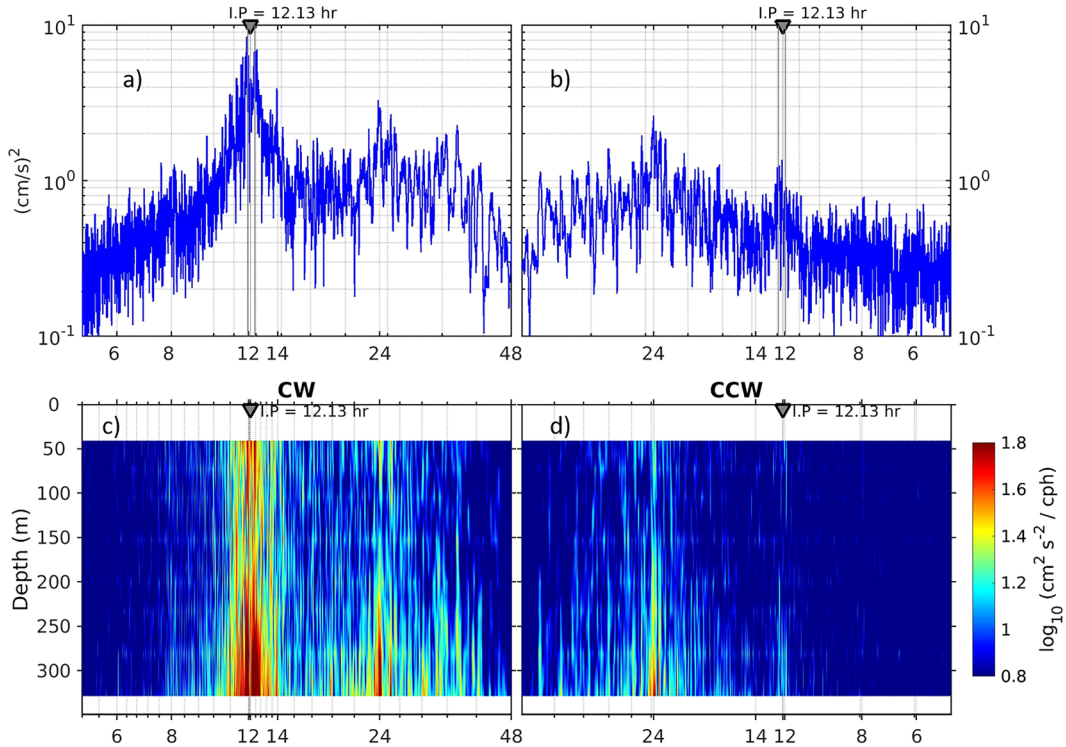

Figure 9. (a, b) Rotary spectra of "baroclinic" velocity time series at 250 m averaging over groups of four adjacent frequencies (2 hr resolution velocities). *x*-axis is period in hour, *y*-axis is energy (in cm^2/s^2). CW, clockwise; CCW, counterclockwise. (c–d) Vertically coordinated frequency spectrum for the complex horizontal "baroclinic" current: left (CW) clockwise rotation and right (CCW) counterclockwise rotation. Periods in hours.

4.2. Velocity Shears in September 2018

We first examined the mesoscale background provided by PSY4 and in situ low frequency velocities. According to PSY4 model, the Yermak Plateau hosted a long-lived anticyclonic eddy from March to mid-October 2018 (Figure 10).

The eddy, with a radius of about 0.5°, had its center wandering in a region between 7E and 8E and between 80.8 and 81.0 N during summer. Thus, the mooring was often outside the eddy (e.g., Figure 10a) and occasionally sampling the anticyclone western edge and its strong northwestward velocities (e.g., Figure 10b) (Artana et al., 2022).

The mooring recorded weak southeastward velocities (<8 cm/s) from September 1 to 9 then strong northwestward flow (>20 cm/s) followed by strong northeastward flow (Figures 11a and 11b). Early September the anticyclonic eddy was away from the mooring which sampled a weak YPB current. The strong flow after 9 September was

Table 3
Selected Cases: Three Winter and Three Summer Months With Minimal Acoustic Doppler Current Profiler Motion (SIC: Sea Ice Concentration, LFOV: Low Frequency Ocean Velocity, MLD: Mixed Layer Depth)

	Winter			Summer		
Dates	March 2018	October 2018	March 2020	September 2018	September 2019	April 2020
SIC %	0	60	100	0	0	100
Winds m/s	Peak > 20	Peaks > 15	Peaks > 15	~10	<10	<10
LFOV cm/s	>25 10	Peak > 30	<10	Peak > 20	0–20	10
MLD m	>600	<50	<50	~80	<10	<20
Comment	Convection	Anticyclone	–	Anticyclone	Anticyclone	–

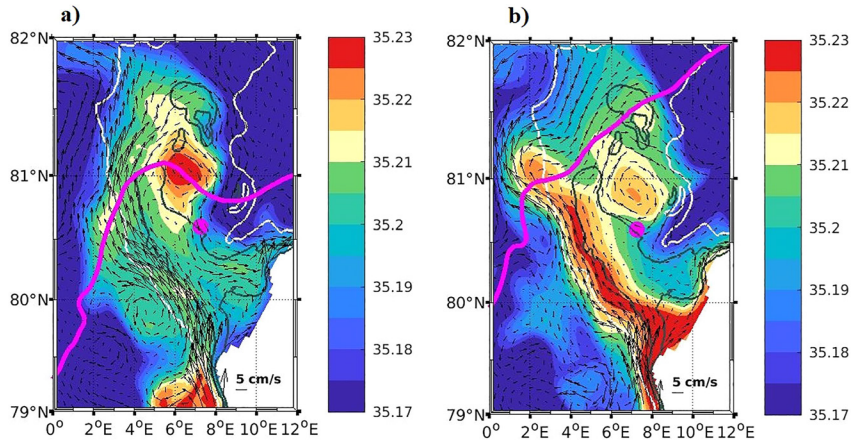

Figure 10. (a) Model Absolute Salinity (SA) (g/kg) at 318 m illustrating times when the mooring was outside the anticyclonic eddy. Arrows indicate velocities at that depth. The magenta contour marks the synoptic ice edge and the white contour the 1,000 isobath. (b) Illustrating times when the mooring recorded northward velocities associated with the western edge of the anticyclone.

associated with the western side of the anticyclonic eddy and concomitant with observed increases in temperature (+1°C) and salinity (+0.07 g/kg) at 345 m leading to a decrease in density (−0.5 kg/m^3) (Figure 11d).

The relative vorticity ζ associated with the eddy was tentatively estimated. ζ can reach values of $-2 * 10^{-5}$ s^{-1} when considering a swirl velocity (from in situ data) of 20 cm/s and an eddy radius of 10 km (estimated from PSY4). The relative vorticity ζ modifies f to an "effective planetary vorticity" ($f_{eff} = f + \zeta/2$) (e.g., Kunze, 1985; Lee & Niiler, 1998). Therefore, f_{eff} could reach values of the order of $2\pi/14$ hr.

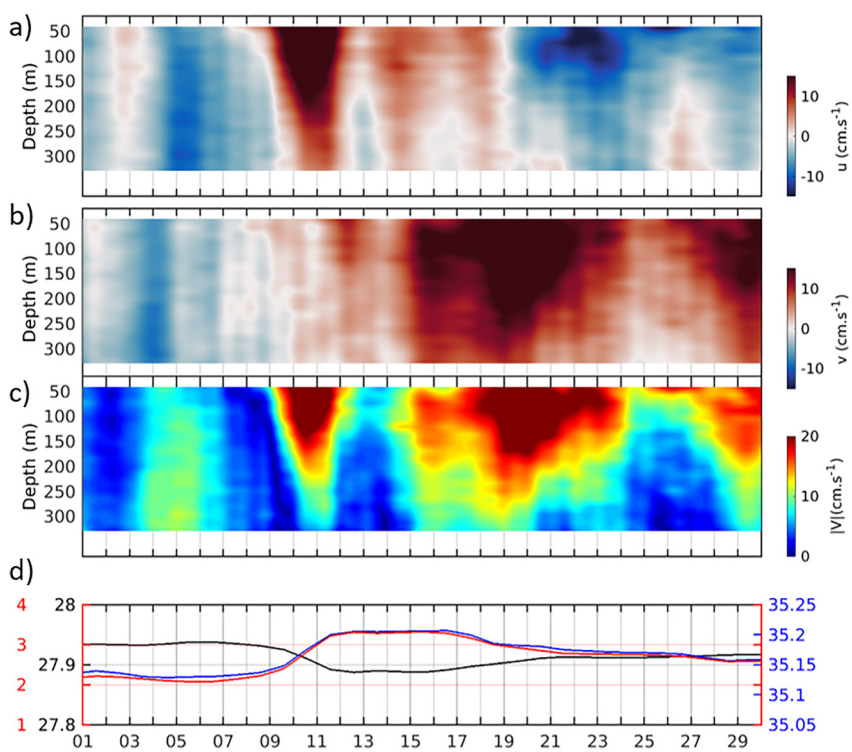

Figure 11. Time series of low-pass (50 hr) filtered data in September 2018: (a) zonal component of velocity from ADCP (50–330 m), (b) meridional component, (c) velocity intensity and (d) absolute salinity (g/kg, in blue), conservative temperature (°C, in red) and potential density (kg/m^3, in black) at 345 m.

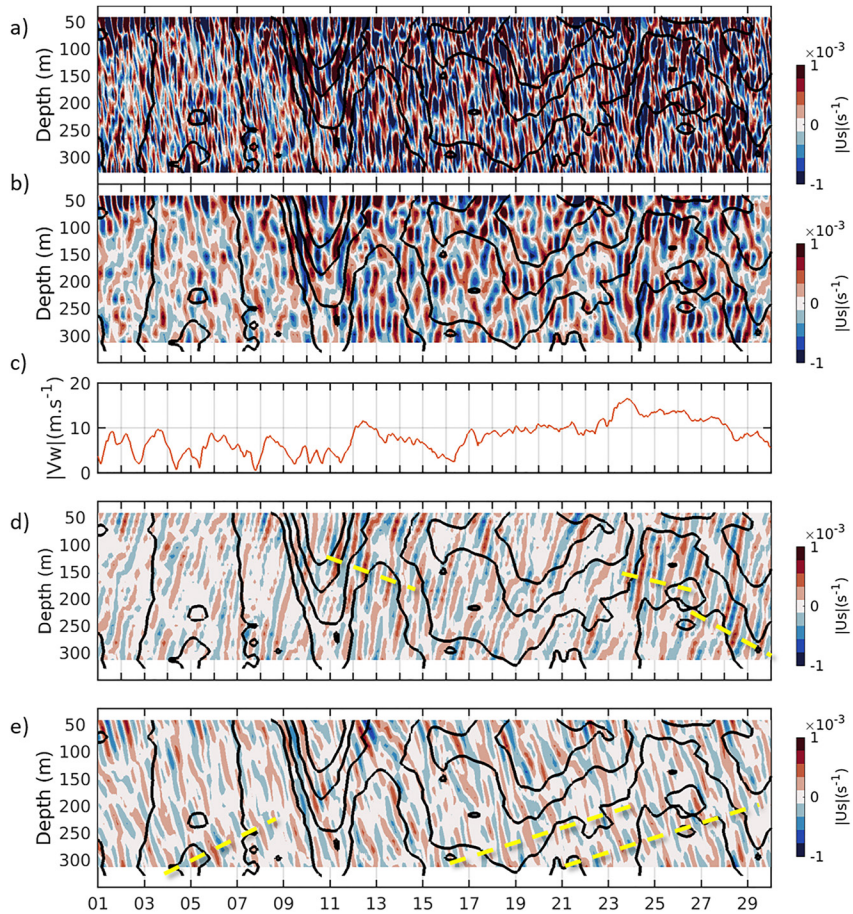

Figure 12. Vertical shear of the 50-hr high-pass filtered zonal velocity (a), stationary component of vertical zonal shear (b), wind intensity (c), downward zonal velocity shear component (d), upward zonal velocity shear component (e) for September 2018. Low-pass filtered velocity amplitude of 5, 10, 15, and 20 cm/s are indicated with black contours in a, b, d and e.

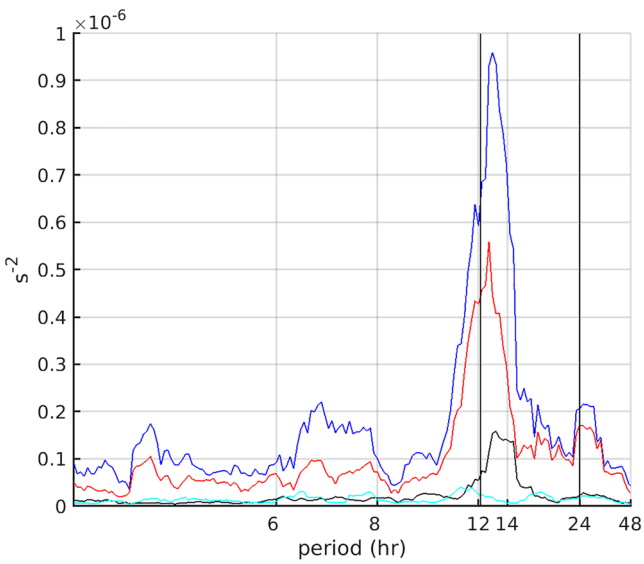

Figure 13. Clockwise spectra of the total shear (blue), stationary component (red), upward component (cyan) and downward component (black) at 180 m for September 2018.

The zonal shear and its three components (upward, downward and stationary) are presented in Figure 12. The meridional shear and its components are shown in Figure S3 in Supporting Information S1. The spectra of the shear components at 180 m are shown in Figure 13.

The amplitude of the vertical shear is strong around 50–60 m depth throughout September. This depth probably corresponds to the base of the mixed layer (Figure 12a). The amplitude of the vertical shear intensifies after 9 September at the time of large low frequency velocities associated with the eddy (Figures 12a and Figure 11c). Most of the energy is concentrated in a broad band around the semi-diurnal period (Figure 13, in blue).

The stationary component amplitude is much larger than the upward and downward propagating shears which are of the same order of magnitude (reaching values of 5×10^{-4} s^{-1}) (Figures 12b, 12d and 12e).

The amplitude of the stationary shears of the high frequency velocity are modulated by the mesoscale background and the low-frequency shears probably associated with changes in the stratification (Figure 11b). The observed modulation of the velocity shear by mesoscale activity is indicative of wave trapping by the anticyclone as a result of the lowering of the planetary vorticity. The stationary shears have variable length scales which are shorter than the upward and downward propagating waves (Figures 12b, 12d, and 12e).

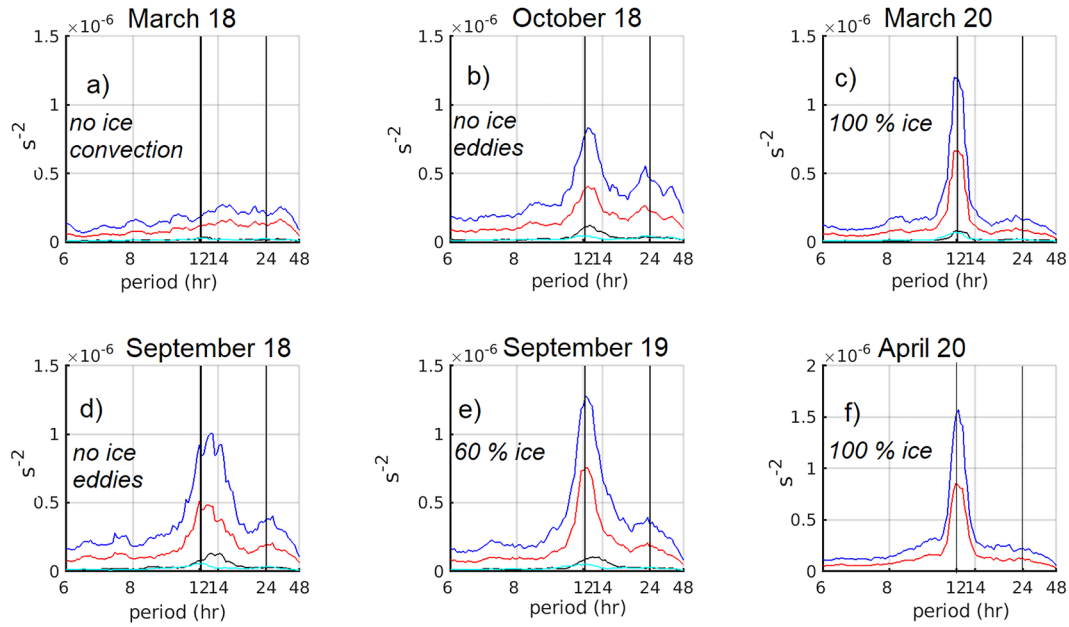

Figure 14. Clockwise spectra of the shear components (total in blue, stationary in red, downward in black and upward in cyan) averaged them vertically for the six selected cases: March 2018 (a), October 2018 (b), March 2020 (c), September 2018 (d), September 2019 (e) and April 2020 (f).

The phase velocity for the downward and upward propagation approximately varies between 150 and 300 m/d. The group velocity is perpendicular to the phase velocity: a downward (upward) energy propagation is associated with an upward (downward) phase propagation. The downward shear energy seems to be modulated by the low frequency flow and by the wind intensity (Figures 12c and 12d). For instance, coherent wave packets propagate downward after September 12 and 23 when intense wind bursts occur (wind peaks >10 m/s). The upward and downward propagation in the water column depends upon the unknown stratification and varies between 10 and 30 m/d (Figures 12d and 12e).

The difference in amplitude between the stationary (red), upward (cyan) and downward (black) propagating shear is striking in the spectra (Figure 13). The spectrum of the stationary shears show concentration of energy around the semi-diurnal period (Figure 13 in red). The small energy of the downward propagating energy is concentrated in a broad band extending to periods of 15 hr (Figure 13, black curve). This is consistent with larger effective inertial period inside anticyclonic eddies. In contrast the very weak upward propagating shear energy is distributed among small peaks at 6.5, 7.5, 11, 17.5, and 24 hr (Figure 13, cyan curve).

4.3. Comparison Between Selected Cases

For the six selected cases identified in Section 2.3 (small ADCP vertical motions) and reported in Table 3 (Section 4.1), we computed spectra of the shear components (total, stationary, downward and upward propagating) at each depth and averaged them vertically (Figure 14). In all spectra, the stationary component (in red) shows energy levels one order of magnitude larger than the vertically propagating components (black and cyan) (Figure 14).

The low energy levels in the March 2018 shear spectra can be explained by the lack of stratification which impeded velocity shear development. Indeed, according to PSY4 model, exceptional mixed layers as deep as 600 m developed at the ice-free mooring location (Figures 4a and 4g) in March 2018. Winter convection is then at play leading to vertically homogeneous water columns (e.g., Athanase et al., 2020).

The other spectra show distinct characteristics according to the absence or presence of mesoscale activity (mainly anticyclonic). The spectra from the two periods with 100% sea ice concentration and no eddies (March 2020 and April 2020, Figures 14c and 14f) exhibit a narrow peak around 12 hr, with the maximum at a smaller period than the inertial period. In contrast, the spectra from the ice-free months or little ice show a broader band energy

distribution around the inertial frequency (Figures 14b, 14d, and 14e). The ice-free months or little ice (October 2018, September 2018 and September 2019, Figures 14b, 14d, and 14e) feature enhanced anticyclonic mesoscale activity (Table 3) which could result from ice-edge eddies (Artana et al., 2022). The frequency broadening likely results from frequency shifts induced by the anticyclonic mesoscale background reducing the planetary vorticity to an effective planetary vorticity as discussed in Section 4.2.

4.4. Possible Physical Interpretation of the Shear Signals

"Baroclinic" velocities and shear spectra (Figures 9, 13, and 14; Figures S1 and S2 in Supporting Information S1) show a dominant peak around the semi-diurnal period while velocity spectra show a dominant peak at the diurnal frequency (Figure 3). This is consistent with recent mooring observations on the southwestern slope of the Yermak Plateau (6E, 79°40') (Wang et al., 2022). Their observations suggest that a strong diurnal barotropic tide impinging on the slope can generate internal waves at higher harmonics, in particular, semi-diurnal internal waves.

In linear theory the direction of IW propagation depends on the stratification (N^2), the frequency (ω) and the Coriolis parameter (f). Topographic slopes can provide resonant wave responses activating waves harmonics. The criticality parameter α ($\alpha = abs(dh/dx)\sqrt{abs\left(N^2-\omega^2\right)/(\omega^2-f^2)}$) is the ratio of topography slope to the slope of energy propagation (Garrett & Kunze, 2007; Legg, 2014). When $\alpha < 1$, the slope is subcritical and only the ω frequency is excited. When $\alpha > 1$ the slope is supercritical generating harmonics of ω. We tentatively computed the critical parameter considering 2K1 and K1 and the slope at the mooring location (Figure 1d). We used several N^2 values, $N^2 = 3.6 * 10^{-6}$ (the reported value in Urbancic et al., 2022 at 1,000 m) and $N^2 = 3.7 * 10^{-7}$ provided by the model at depth. In both cases, the topography is critical or close to critical for 2K1 (1.45 and 0.65) while it is subcritical for K1 (0.1). In spite of the uncertainties in the critical parameter estimate, linear theory predicts possible generation of internal waves at the semi-diurnal period at the mooring location, and, could explain the dominance of the semi-diurnal period in the shear spectra. While M2 period (12.42 hr) is larger than the inertial period (12.13 hr), 2K1 period (11.97 hr) is smaller. Therefore internal waves with 2K1 period can freely propagate, while those with M2 period dissipate locally in the absence of a strong local background vorticity.

Using a numerical study Urbancic et al. (2022) show that strong diurnal barotropic tides over steep slopes can lead to the generation of linear and nonlinear internal waves with 2K1 period and in particular of Internal Solitary Waves. When the tidal currents are larger than 0.14 m/s their model produces Internal Solitary Waves in the northern Yermak Plateau where the slope is steep (Figure 1b) and does not in the southwestern Yermak Plateau where slope is smoother. Solitary Waves were observed in in-situ data and SAR images over the steep slope of Northeast Svalbard at the time of strong diurnal tidal currents (Fer et al., 2020). Solitary Waves are not expected at the mooring location since the slope is relatively gentle (Figures 1b and 1d) and SAR images did not show any particular signal in this region (Kozlov et al., 2015).

The generating mechanism of stationary waves at the mooring location deserves further investigation. Possibly, interactions of freely propagating internal waves at period 2K1 (11.97 hr) generated and propagated from both eastern and western slopes of the rather narrow plateau could lead to stationary waves as observed here. Further moorings in the Yermak Plateau complementing observations by Wang et al. (2022) on the southwestern slope and the present ones on the eastern slope are needed to test this hypothesis.

5. Summary and Conclusions

We examined high frequency velocity variations in 3 years-long velocity records gathered in the Yermak Pass. While the region used to be ice-covered, the mooring site was ice-free half of the time (including summer and winter). High frequencies (periods less than 50 hr) account for more than 70% of the total velocity variance. The length of the time series allowed to distinguish between the tidal harmonics. A tidal decomposition showed the dominance of diurnal harmonics (K1, O1, P1) over the semi-diurnal component (M2, S2, N2). The Arc5km2018 tide model provided tidal constituents satisfactorily matching those derived from the observations in spite of the rather complex bathymetry in the vicinity of the mooring. Arc5km2018 model highlighted locations of the plateau with particularly large tidal currents such as the plateau crest and the northern tip of the Plateau in agreement with the scarce observations recalled in Padman et al. (1992).

Twin simulations (1/36° resolution with and without tides) revealed residual tidal currents, leading to the generation of time-mean anticyclonic circulation around the Yermak Plateau, thus confirming Padman et al. (1992)'s hypothesis. The twin simulations hinted that the diurnal tide likely is the main contributor to rectification and mixing leading to the residual currents. The simulations led to residual current speeds up to 7 cm/s in the northern plateau (3 cm/s on the eastern side of the plateau), values that are larger than (comparable with) mean background currents in the region. The rectified circulation and mixing induced by tides may be a particularly important mechanism for AW transport around the northern tip of the plateau.

The twin simulations suggested that the residual tidal velocities were opposite to the mean flow direction in the Yermak Pass and in particular at the mooring location in agreement with estimates obtained by Koenig et al. (2017) comparing velocities from an operational model with no tides (PSY4) and mooring velocities. Thus, the YPB transport derived from a model without tides may be overestimated.

Overall, this exploratory comparison advocates taking tides into account when examining low-frequency AW inflow. Tidal residual currents in the region deserve dedicated investigation. In particular, further studies are needed to investigate changes in residual currents associated with variations in stratification and mean flow. Indeed, Skarðhamar et al. (2015) showed that diurnal tides on the Barents Sea continental slope vary in response to changing stratification and mean flow.

We next examined vertical shears using the ADCP data. We decomposed velocity shears into stationary, upward and downward propagating components using Park et al. (2004) methodology. The stationary shear energy was an order of magnitude larger than the downward and upward propagating shear energy. Occasionally wind-forced downward propagating waves were generated with variable group velocities. Most of the shear energy was found in a broad band around the inertial frequency (Figures 9, 13, and 14; Figures S1 and S2 in Supporting Information S1). Thus, the shear energy is smaller at the diurnal period than at the semi-diurnal period, in contrast with the velocity energy (Figure 3). The energy concentration around the semi-diurnal band can be explained by the generation of internal waves at the 2K1 period (11.97 hr) forced by the diurnal tides over critical slopes around the plateau. These waves can freely propagate, in contrast to M2 and K1 which have periods larger than the local inertial period (12.13 hr). Interaction of internal waves at 2K1 period could be a key factor in the generation of the stationary shears around the inertial period.

We observed enhancement of the shear amplitude in the presence of eddies and modulation of the shear velocity signals by the mesoscale background suggesting wave trapping. Indeed, as a result of the lowering of the inertial frequency, waves become superinertial and can be trapped inside the anticyclonic eddies (Kunze et al., 1995). In the ice-free study cases, the relative vorticity associated with anticyclonic eddies, possibly ice-edge eddies, led to a larger effective planetary period broadening the energetic frequency band. In contrast, during ice covered periods the velocity shear spectra showed a narrow peak around 12 hr in the absence of anticyclone.

We documented the predominance of stationary shears around the inertial period at the mooring location that probably results from the transfer of strong diurnal barotropic tides to semi-diurnal internal waves. Further observations are needed to confirmed this hypothesis. Internal waves in a varying stratification environments undergo changes in their amplitude and wavelength.The lack of observed stratification profiles in a region where stratification is highly variable (Text S4 in Supporting Information S1) restrained the analysis.

These observed stationary waves with short length scales are susceptible to break and generate mixing (e.g., D'Asaro & Morison, 1992; Fer, 2014; Fer et al., 2020; Padman & Dillon, 1991; Rippeth et al., 2017) which is important for heat and momentum balances at the entrance of the Atlantic Water to the Arctic.

Appendix A: 50-Hr High-Pass Filtered Mooring Data-Mooring Motions

The mooring stayed straight and the standard deviation of the microcat pressure is less than 2 db (Figure A1). However, the pressure spectrum shows distinct significant peaks (above 95% CL) at high frequencies with amplitude of 4.5 db around 24 hr (23.93 and 25.82 hr, i.e., K1 and O1 tidal constituents) and less than 3db around periods of 12 (12.42 hr M2 constituent and 12.13 hr inertial period), 8.2 and 6.2 hr (Figure A2). Those periods were observed in velocity spectral peaks (Figure 3). We selected six study cases with small pressure variations (Section 2.3 and Figure 4).

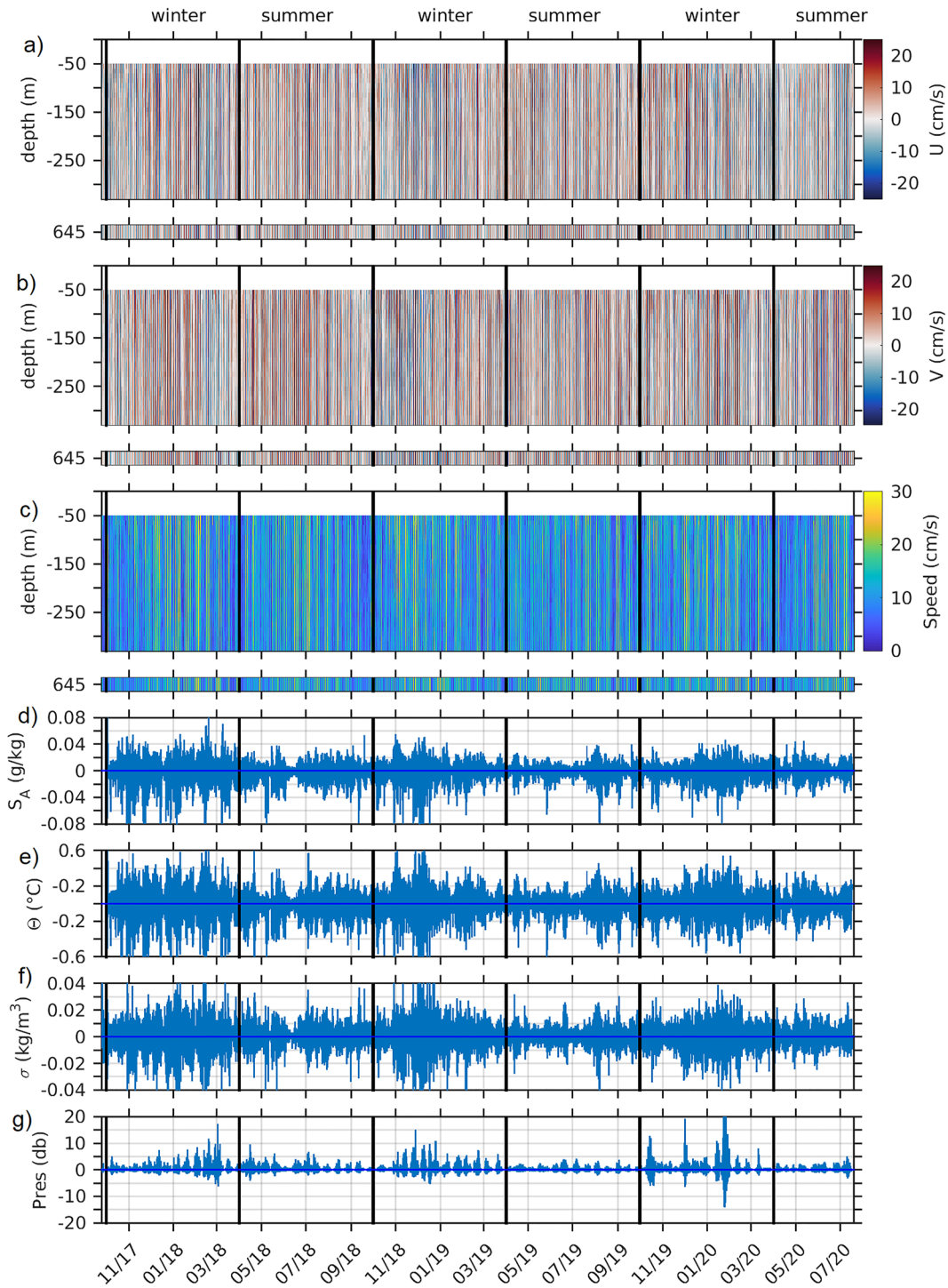

Figure A1. Fifty-hour high-pass filtered time series of: (a) zonal component of velocity from Acoustic Doppler Current Profiler (ADCP) (50–330 m profiles) and Aquadopp at 645 m, (b) meridional velocity component (ADCP and Aquadopp), and (c) horizontal speed (ADCP and Aquadopp), (d) absolute salinity, (e) potential temperature, (f) potential density and (g) pressure. (Summer: April–September, winter: October–March).

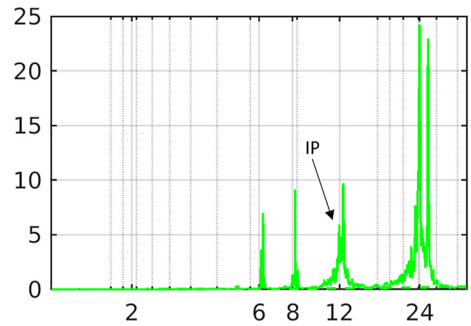

Figure A2. Spectral content averaging over groups of 10 adjacent frequencies (sampling time 10 min) of pressure. *x*-axis is period in hr and *y*-axis $(db)^2$. The dotted line-close to the *x*-axis-shows the 95% confidence interval. IP stands for inertial period: 12.13 hr.

Data Availability Statement

The raw and 50 hr high-pass filtered mooring data are available in the SEANOE data base: https://doi.org/10.17882/89349 and the 50 hr low-pass filtered mooring data at https://doi.org/10.17882/83214. The model outputs are available at: Copernicus Marine Environment Monitoring Service (CMEMS; http://marine.copernicus.eu).

Acknowledgments
We are deeply grateful to the officers, crews and scientists onboard the Norvegian Research Vessel Lance (deployment) and Norwegian ice breaker KV Svalbard (recovery). We thank A. Sundfjord and J.C. Gascard for their constant support and help. Matthieu Labaste (LOCEAN) was instrumental in mooring preparation and logistics. The field work was funded through the ANR EQUIPEX IAOOS project through ANR-10-EQX-32-01 grant and the ICE-ARC programme from the European Union 7th Framework Programme, Grant 603887. We acknowledge the two reviewers and the editor for their comments and suggestions. Camila Artana acknowledges funding from the Spanish government (AEI) through the "Severo Ochoa Centre of Excellence" accreditation (CEX2019-000928-S) and Lea Poli from a Sorbonne Université Ph.D. scolarship. This work is a contribution to H2020 Arctic Passion project, Grant 101003472. The Mercator ocean global operational system is part of the Copernicus Marine Environment Monitoring Service (CMEMS; http://marine.copernicus.eu).

References

Alford, M. H., MacKinnon, J. A., Simmons, H. L., & Nash, J. D. (2016). Near-inertial inertial gravity waves in the ocean. *Annual Review of Marine Science*, *8*(1), 95–123. https://doi.org/10.1146/annurev-marine-010814-015746

Arbic, B. K., Garner, S. T., Hallberg, R. W., & Sim-mons, H. L. (2004). The accuracy of surface elevations in for-ward global barotropic and baroclinic tide models. *Deep-Sea Research*, *51*(25–26), 3069–3101. https://doi.org/10.1016/j.dsr2.2004.09.014

Artana, C., Provost, C., Koenig, Z., Athanase, M., & Asgari, A. (2022). Atlantic water inflow through the Yermak Pass branch: Evolution since 2007. *Journal of Geophysical Research: Oceans*, *127*(2), e2021JC018006. https://doi.org/10.1029/2021JC018006

Athanase, M., Provost, C., Artana, C., Pérez-Hernández, M. D., Sennéchael, N., Bertosio, C., et al. (2021). Changes in Atlantic water circulation patterns and volume transports north of Svalbard over the last 12 years (2008–2020). *Journal of Geophysical Research: Oceans*, *126*(1), e2020JC016825. https://doi.org/10.1029/2020JC016825

Athanase, M., Provost, C., Pérez-Hernández, M. D., Sennéchael, N., Bertosio, C., Artana, C., et al. (2020). Atlantic water modification north of Svalbard in the Mercator physical system from 2007 to 2020. *Journal of Geophysical Research: Oceans*, *125*(10), e2020JC016463. https://doi.org/10.1029/2020JC016463

Athanase, M., Sennéchael, N., Garric, G., Koenig, Z., Boles, E., & Provost, C. (2019). New hydrographic measurements of the upper Arctic Western Eurasian Basin in 2017 reveal fresher mixed layer and shallower warm layer than 2005–2012 climatology. *Journal of Geophysical Research: Oceans*, *124*(2), 1091–1114. https://doi.org/10.1029/2018JC014701581

Crews, L., Sundfjord, A., & Hattermann, T. (2019). How the Yermak pass branch regulates Atlantic water inflow to the Arctic Ocean. *Journal of Geophysical Research: Oceans*, *124*(1), 267–280. https://doi.org/10.1029/2018JC014476

D'Asaro, E. A., & Morison, J. H. (1992). Internal waves and mixing in the Arctic Ocean. *Deep-Sea Research*, *39*(2), S459–S484. https://doi.org/10.1016/S0198-0149(06)80016-6

Dosser, H. V., & Rainville, L. (2016). Dynamics of the changing near-inertial internal wave field in the Arctic Ocean. *Journal of Physical Oceanography*, *46*(2), 395–415. https://doi.org/10.1175/JPO-D-15-0056.1

Erofeeva, S., & Egbert, G. (2020). Arc5km2018: Arctic ocean inverse tide model on a 5 kilometer grid, (2018) [Dataset]. Arctic Data Center. https://doi.org/10.18739/A21R6N14K

Fer, I. (2014). Near-inertial mixing in the central Arctic Ocean. *Journal of Physical Oceanography*, *44*(8), 2031–2049. https://doi.org/10.1175/JPO-D-13-0133.1

Fer, I., Koenig, Z., Kozlov, I. E., Ostrowski, M., Rippeth, T. P., Padman, L., et al. (2020). Tidally forced lee waves drive turbulent mixing along the Arctic Ocean margins. *Geophysical Research Letters*, *47*(16), e2020GL088083. https://doi.org/10.1029/2020GL088083

Fer, I., Müller, M., & Peterson, A. K. (2015). Tidal forcing, energetics, and mixing near the Yermak Plateau. *Ocean Science*, *11*(2), 287–304. https://doi.org/10.5194/os-11-287-2015615

Foreman, M. G. G. (1978). Manual for tidal currents analysis and prediction. In *Pacific marine science report 78-6* (p. 57). Institute of Ocean Sciences.

Garrett, C., & Kunze, E. (2007). Internal tide generation in the deep ocean. *Annual Review of Fluid Mechanics*, *39*(1), 57–87. https://doi.org/10.1146/annurev.fluid.39.050905.110227

Guthrie, J. D., & Morison, J. H. (2020). Not just sea-ice: Other factors important to near-inertial wave generation in the Arctic Ocean. *Geophysical Research Letters*, *48*(3), e2020GL090508. https://doi.org/10.1029/2020GL090508

Guthrie, J. D., Morison, J. H., & Fer, I. (2013). Revisiting internal waves and mixing in the Arctic Ocean. *Journal of Geophysical Oceanography*, *118*(8), 3966–3977. https://doi.org/10.1002/jgrc.20294

Hunkins, K. (1986). Anomalous diurnal tidal currents on the Yermak Plateau. *Journal of Marine Research*, *44*(1), 51–69. https://doi.org/10.1357/002224086788460139

Jackson, C. R., Da Silva, J. C., & Jeans, G. (2012). The generation of nonlinear internal waves. *Oceanography*, *25*(2), 108–123. https://doi.org/10.5670/oceanog.2012.46

Jakobsson, M., Mayer, L., Coakley, B., Dowdeswell, J. A., Forbes, S., Fridman, B., et al. (2012). The international bathymetric chart of the Arctic Ocean (IBCAO) version 3.0. *Geophysical Research Letters*, *39*(12), L12609. https://doi.org/10.1029/2012GL052219

Koenig, Z., Provost, C., Sennéchael, N., Garric, G., & Gascard, J.-C. (2017). The Yermak Pass Branch: A major pathway for the Atlantic water north of Svalbard? *Journal of Geophysical Research: Oceans*, *122*(12), 9332–9349. https://doi.org/10.1002/2017JC013271

Kozlov, I. E., Kudryavtsev, V. N., Zubkova, E. V., Atadzhanova, O., Zimin, A. V., Romanenkov, D., et al. (2015). SAR observations of internal waves in the Russian Arctic seas. In *IEEE international geoscience and remote sensing symposium (IGARSS)* (pp. 947–949). https://doi.org/10.1109/IGARSS.2015.7325923

Kunze, E. (1985). Near-inertial wave propagation in geostrophic shear. *Journal of Physical Oceanography*, *15*(5), 544–565. https://doi.org/10.1175/1520-0485(1985)015<0544:NIWPIG>2.0.CO;2

Kunze, E., Schmidt, R. W., & Toole, J. M. (1995). The energy balance in a warm core ring's near-inertial critical layer. *Journal of Physical Oceanography*, *25*(5), 942–957. https://doi.org/10.1175/1520-0485(1995)025<0942:TEBIAW>2.0.CO;2

Lee, D. K., & Niiler, P. P. (1998). The inertial chimney: The near-inertial energy drainage from the ocean surface to the deep layer. *Journal of Geophysical Research*, *103*(C4), 7579–7591. https://doi.org/10.1029/97JC03200

Legg, S. (2014). Scattering of low-mode internal waves at finite isolated topography. *Journal of Physical Oceanography*, *44*(1), 359–383. https://doi.org/10.1175/JPO-D-12-0241.1

Lellouche, J.-M., Greiner, E., Le Galloudec, O., Garric, G., Regnier, C., Drevillon, M., et al. (2018). Recent updates on the Copernicus Marine Service global ocean monitoring and forecasting real-time 1/12 high resolution system. *Ocean Science*, *14*(5), 1093–1126. https://doi.org/10.5194/os-2018-15

Lincoln, B. J., Rippeth, T. P., Lenn, Y.-D., Timmermans, M. L., Williams, W. J., & Bacon, S. (2016). Wind-driven mixing at intermediate depths in an ice-free Arctic Ocean. *Geophysical Research Letters*, *43*(18), 9749–9756. https://doi.org/10.1002/2016GL070454

Loder, J. W. (1980). Topographic rectification of tidal currents on the sides of Georges Bank. *Journal of Physical Oceanography*, *10*(9), 1399–1416. https://doi.org/10.1175/1520-0485(1980)010<1399:TROTCO>2.0.CO;2

Martini, K. I., Simmons, H. L., Stoudt, C. A., & Hutchings, J. K. (2014). Near-inertial waves and sea-ice in the Beaufort Sea. *Journal Physical Oceanography*, *44*(8), 2212–2234. https://doi.org/10.1175/JPO-D-13-0160.1

Merrifield, M. A., & Pinkel, R. (1996). Inertial currents in the Beaufort Sea: Observations of response to wind and shear. *Journal of Geophysical Research*, *101*(C3), 6577–6590. https://doi.org/10.1029/95JC03625

Nagai, T., Tandon, A., Kunze, E., & Mahadevan, A. (2015). Spontaneous generation of near-inertial waves from the Kuroshio Front. *Journal of Physical Oceanography*, *45*(9), 2381–2406. https://doi.org/10.1175/JPO-D-14-0086.1

Nakamura, T., & Awaji, T. (2001). A growth mechanism for topographic internal waves generated by an oscillatory flow. *Journal of Physical Oceanography*, *31*(8), 2511–2524. https://doi.org/10.1175/1520-0485(2001)031<2511:AGMFTI>2.0.CO;2

Nikurashin, M., & Ferrari, R. (2010). Radiation and dissipation of internal waves generated by geostrophic flows impinging on small-scale topography: Theory. *Journal of Physical Oceanography*, *40*(5), 1055–1074. https://doi.org/10.1175/2009JPO4199.1

Padman, L., & Dillon, T. (1991). Turbulent mixing near the Yermak Plateau during the coordinated Eastern Arctic Experiment. *Journal Geophysical Research, Oceans*, *96*(C3), 4769. https://doi.org/10.1029/90JC02260

Padman, L., Plueddemann, A. J., Muench, R. D., & Pinkel, R. (1992). Diurnal tides near the Yermak Plateau. *Journal Geophysical Research, Oceans*, *97*(C8), 12639. https://doi.org/10.1029/92JC01097

Park, Y.-H., Roquet, F., & Vivier, F. (2004). Quasi-stationary ENSO wave signals versus the Antarctic Circumpolar Wave scenario. *Geophysical Research Letters*, *31*(9), L09315. https://doi.org/10.1029/2004GL019806

Pawlowicz, R., Beardsley, B., & Lentz, S. (2002). Classical tidal harmonic analysis including error estimates in MATLAB using T_TIDE. *Computers & Geosciences*, *28*(8), 929–937. https://doi.org/10.1016/S0098-3004(02)00013-4

Plueddemann, A. J. (1992). Internal wave observations from the Arctic environmental drifting buoy. *Journal of Geophysical Research*, *97*(C8), 12619. https://doi.org/10.1029/92JC01098

Rainville, L., & Woodgate, R. A. (2009). Observations of internal wave generation in the seasonally ice-free Arctic. *Geophysical Research Letters*, *36*(23), L23604. https://doi.org/10.1029/2009GL041291

Rippeth, T. P., Vlasenko, V., Stashchuk, N., Scannell, B. D., Green, J. A. M., Lincoln, B. J., & Bacon, S. (2017). Tidal conversion and mixing poleward of the critical latitude (an Arctic case study). *Geophysical Research Letters*, *44*(24), 12349–12357. https://doi.org/10.1002/2017GL075310

Skarðhamar, J., Skagseth, Ø., & Albretsen, J. (2015). Diurnal tides on the Barents Sea continental slope. *Deep Sea Research Part I: Oceanographic Research Papers*, *97*, 40–51. https://doi.org/10.1016/j.dsr.2014.11.008

Urbancic, G. H., Lamb, K. G., Fer, I., & Padman, L. (2022). The generation of linear and nonlinear internal waves forced by subinertial tides over the Yermak Plateau, Arctic Ocean. *Journal of Physical Oceanography*, *52*(9), 2183–2203. https://doi.org/10.1175/JPO-D-21-02164.1

Vlasenko, V., Stashchuk, N., Hutter, K., & Sabinin, K. (2003). Nonlinear internal waves forced by tides near the critical latitude. *Deep Sea Research Part I: Oceanographic Research Papers*, *50*(3), 317–338. https://doi.org/10.1016/S0967-0637(03)00018-9

Wang, S., Cao, A., Li, Q., & Chen, X. (2022). Diurnal and semidiurnal internal waves on the southern slope of the Yermak Plateau. *Scientific Reports*, *12*(1), 11682. https://doi.org/10.1038/s41598-022-15661-0

Wright, D. G., & Loder, J. W. (1985). A depth-dependent study of the topographic rectification of tidal currents. *Geophysical & Astrophysical Fluid Dynamics*, *31*(3–4), 169–220. https://doi.org/10.1080/03091928508219269

Zimmerman, J. T. F. (1978). Topographic generation of residual circulation by oscillatory (tidal) currents. *Geophysical & Astrophysical Fluid Dynamics*, *11*(1), 35–47. https://doi.org/10.1080/03091927808242650

References From the Supporting Information

Leaman, K. D., & Sanford, T. B. (1975). Vertical energy propagation of inertial waves: A vector spectral analysis of velocity profiles. *Journal of Geophysical Research*, *80*(15), 1975–1978. https://doi.org/10.1029/JC080i015p01975